Electronic structure and transport properties in the transparent amorphous oxide semiconductor $2\,CdO{\cdot}GeO_2$

Satoru Narushima
Materials and Structures Laboratory, Tokyo Institute of Technology, Nagatsuta, Midori-ku, Yokohama 226-8503, Japan

Masahiro Orita and Masahiro Hirano
Transparent ElectroActive Materials, Exploratory Research for Advanced Technology, Japan Science and Technology Corporation, KSP C-1232, 3-2-1 Sakado, Takatsu-ku, Kawasaki 213-0012, Japan

Hideo Hosono*
Materials and Structures Laboratory, Tokyo Institute of Technology, Nagatsuta, Midori-ku, Yokohama 226-8503, Japan and Transparent ElectroActive Materials, Exploratory Research for Advanced Technology, Japan Science and Technology Corporation, KSP C-1232, 3-2-1 Sakado, Takatsu-ku, Kawasaki 213-0012, Japan

(Received 31 October 2001; revised manuscript received 4 March 2002; published 16 July 2002)

An amorphous $2\,CdO{\cdot}GeO_2$ thin film with a band gap of 3.4 eV can be converted from an insulator (conductivity $\sim 10^{-9}$ S cm^{-1}) into a degenerate semiconductor ($\sim 10^{2}$ S cm^{-1}) by carrier doping with ion implantation without significant loss in visible transparency. An interesting feature of this material's transport property is its Hall mobility: a *pn* sign anomaly, which is commonly observed for amorphous semiconductors, is not seen. The estimated Hall mobility is ~ 10 cm^2 V^{-1} s^{-1}, which is larger by several orders of magnitude than that of conventional amorphous semiconductors, and is comparable to that in the polycrystalline form. The electronic structure was investigated to understand these features through direct observation of the density of states (DOS) of the conduction band by inverse-photoelectron spectroscopy and molecular orbital calculation of the DOS for a model cluster justified by x-ray structural analysis combined with molecular dynamics and reverse Monte Carlo simulations. Although x-ray structural analysis revealed that disorder in the correlation between Cd-Cd ions was distinctly seen in the amorphous state, the DOS of the conduction band bottom was almost the same in the crystalline and amorphous states. Cluster calculations demonstrated that the bottom of the conduction band is primarily composed of Cd 5*s* orbitals. The characteristic transport properties in this material, such as large electron mobility, may be understood by considering that the magnitude of overlap between the 5*s* orbitals of neighboring Cd^{2+} is large and comparable to that in the crystal and insensitive to the structural randomness inherent to amorphous states.

DOI: 10.1103/PhysRevB.66.035203 PACS number(s): 61.43.Bn, 71.23.Cq, 79.60.Ht

I. INTRODUCTION

Demand for transparent conductive oxides (TCOs) is increasing in technical applications such as transparent electrode materials for liquid crystal displays (LCDs) and solar cells. A few crystalline oxides such as tin-doped indium oxide (ITO) and SnO_2 are used for those purposes. On the other hand, amorphous materials exhibiting both visible transparency and high electrical conductivity have unique advantages over the crystalline TCOs. For example, low-temperature deposition on plastic substrates for LCDs is possible.[1] A series of amorphous semiconductors, such as the tetrahedral systems represented by amorphous (*a*-) Si, chalcogenide and oxide glasses containing 3*d*-mixed-valence cations, are known to exist, but they do not meet both high optical transparency and high conductivity.

We recently found amorphous transparent conductive materials in several double oxide systems: *a*-$AgSbO_3$,[2] *a*-$2CdO{\cdot}GeO_2$,[3] *a*-$CdO{\cdot}PbO_x$[4] and *a*-$InGaO_3(ZnO)_m$ ($m \leqslant 4$).[5] Those materials and *a*-ITO_x[6–8] have been characterized by the unique electronic transport properties, i.e., high electron mobility comparable to that in corresponding crystalline materials and the absence of the *pn* sign anomaly in the Hall coefficient which is commonly observed in amorphous semiconductors.

These amorphous TCOs were found based on our own working hypothesis, that is, *s*-band conductors are suitable to obtain large electron mobilities even in the amorphous state. The magnitude of the overlap between relevant *s* orbitals is insensitive to the structural randomness inherent to the amorphous state because the shape of the *s* orbital is spherical. Therefore, band dispersion at the conduction band bottom in the amorphous state is comparable to that in the crystal state. Also, the spatial spreading of the *ns* orbitals that constitute the conduction band must be large enough. In this category of TCO systems, *n* is more than 5 except for *a*-$InGaO_3(ZnO)_m$ ($m \leqslant 4$). Amorphous $2\,CdO{\cdot}GeO_2$ is representative of these TCOs.

Amorphous $2\,CdO{\cdot}GeO_2$, with a band gap of 3.4 eV, is optically transparent and electrically insulating with a conductivity of $\sim 10^{-9}$ S cm^{-1} at $\sim$300 K, but it can be converted into an *n*-type degenerate semiconductor (conductivity 10^{1}–10^{2} S cm^{-1}) by carrier doping via ion implantation of protons without significant loss in visible transparency. The doping was effective without post annealing to activate the dopant. The conductivity can be controlled continuously over 10^{-9}–10^{2} S cm^{-1} by varying the fluence,[9] indicating that the Fermi level is controllable by doping. This is the interesting feature of amorphous $2\,CdO{\cdot}GeO_2$. Negative

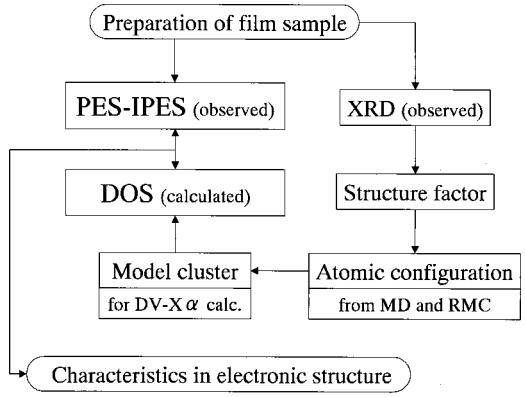

FIG. 1. Approach to elucidation of electronic structure in amorphous 2 $CdO \cdot GeO_2$. XRD: x-ray diffraction, RMC: reverse Monte Carlo simulation, PES-IPES: photoelectron and inverse photoelectron spectroscopy.

signs of the Hall and Seebeck coefficients were observed, showing that the primary charge carrier is an electron. On the assumption that each implanted proton generates a carrier electron ($H \rightarrow H^+ + e_{cond}$), the carrier generation efficiency is calculated to be $\sim 10\%$ (H^+, 2×10^{16} cm^{-2}).[9] The so-called "*pn* anomaly" in the Hall voltage is not seen for the material. The electron mobility in the degenerated state is ~ 10 $cm^2 V^{-1} s^{-1}$, which is larger by several orders of magnitude than the values in existing amorphous semiconductors [i.e., $\sim 10^{-4}$ $cm^2 V^{-1} s^{-1}$ for *a*-As_2S_3 (Ref. 10) and $\sim 10^{-1}$ $cm^2 V^{-1} s^{-1}$ for *a*-Si:H (Ref. 11)]. Furthermore, this value is almost the same as that (8–15 $cm^2 V^{-1} s^{-1}$) (Ref. 12) in polycrystalline Cd_2GeO_4 which is known to be an *n*-type conductor.

A way to examine the behavior of free carriers is to analyze the optical conductivity. In a previous paper,[13] we analyzed the optical absorption due to free carrier electrons in the present material (degenerated state) by the Drude approach, evaluating fundamental parameters associated with electron transport, i.e., effective mass of $0.33m_0$ and mean free path of 1.4 nm. The value of mean free path is close to those in liquid metals[14] and is significantly larger than the bond distance.

The purpose of the present study is to consider the origin of these properties through elucidation of the electronic structure. Figure 1 summarizes the present approach. The density of states (DOS) in the vicinity of the band gap is elucidated by combining the spectroscopic measurements with the molecular orbital (MO) calculations. Ultraviolet photoelectron (PE) and ultraviolet inverse photoelectron (IPE) spectroscopies were employed to directly observe the DOS of the valence band and conduction band, respectively. For disordered matter, a molecular orbital calculation is effective to analyze the PE-IPE spectra. An appropriately modeled cluster is required for the calculation. The structures of model clusters were determined through the combined use of molecular dynamics (MD) simulations and reverse Monte Carlo (RMC) analysis of the observed x-ray diffraction data. Finally, the DOS was calculated by MO calculations on the model cluster and compared with the observed DOS.

II. EXPERIMENTAL

A. Sample preparation

Film samples were prepared by the rf sputtering method using a sintered disk of polycrystalline Cd_2GeO_4 as a target under an atmosphere of $Ar/O_2 = 4/1$.[3] A plate of SiO_2 glass was used as a substrate and was not intentionally heated during deposition.

Protons were implanted into the as-deposited film at ambient temperature to a fluence of 2×10^{16} cm^{-2}. Two-step acceleration voltages (1×10^{16} cm^{-2} at 40 kV $\rightarrow$ 1×10^{16} cm^{-2} at 70 kV) were employed to avoid large concentration of implanted ions near the stopping range. The sample was wrapped with Al foil except portions to be implanted to reduce charging during implantation. The depth profile of the implanted protons was calculated using the transport of ions matter (TRIM-94) code.[15] Two-energy-level proton implantation processes lead to a calculated profile with two peaks at 300 and 450 nm from the top surface. The experimental depth profile of protons by secondary-ion mass spectrometry (SIMS) was very broad and peaked at ~ 100 nm from the film surface, and the proton concentration was decreased to half of the peak at the bottom surface (~ 650 nm), i.e., the concentration ratio between the peak and the near the surfaces remains ~ 2.[16] The dose rate was 2.4×10^{12} ions $cm^{-2} s^{-1}$. No post annealing was performed after the ion implantation.

Chemical compositions of the films were determined by inductively coupled plasma emission (ICP) spectroscopy after the samples were dissolved in acid solution. The amorphous nature of resulting films was confirmed by selected-area electron diffraction (SAED) patterns under cross-sectional transmission electron microscopy (TEM) observation.

B. Photoelectron spectroscopy

Photoelectron spectroscopy and inverse photoelectron spectroscopy were performed on the H^+-implanted conductive amorphous $2CdO \cdot GeO_2$ film. The film thickness was ~ 650 nm. For comparison, PE-IPE spectra were also measured on a polycrystalline disk of Cd_2GeO_4. The disk was prepared by the following procedures. The Cd_2GeO_4 powder, synthesized by solid state reaction of CdO and GeO_2 at 850 °C, was unidirectionally pressed into a disk. After cold-isostatic pressing at a pressure of ~ 300 MPa, the disk was sintered at 850 °C for 8 h. The disk was conductive. A Hall mobility of ~ 10 $cm^2 V^{-1} s^{-1}$ was reported both for the amorphous film and the polycrystal.[3,12] Measurements of PE and IPE spectra were carried out with a laboratory-made spectrometer which was composed of three UHV chambers for PE, IPE, and sample preparation (base pressure $< 10^{-8}$ Pa).

For PE measurements, a He discharge lamp with 40.8 eV line (He II) was used as the excitation source. Electrons emitted from the sample were analyzed with a hemispherical analyzer (VSW CLASS150). The energy resolution of PE spectra was 0.12 eV.

Ultraviolet IPE measurements were performed in the bremsstrahlung isochromat spectroscopy (BIS) mode. An

electron beam from an electron gun was focused onto the sample and the emission of VUV light (9.45 eV) from the sample was detected by the band-pass photon detector. The energy resolution of IPE spectra was 0.45 eV. The energy calibration of the spectra was performed by measuring the spectrum of gold.

C. X-ray diffraction measurement

X-ray diffraction measurements were carried out with Mo $K\alpha$ radiation (50 kV−40 mA) from a diffractometer (Rigaku RINT 1200, Japan). The sample used was a ~15-μm-thick film deposited on a glass plate by sputtering. This thickness was chosen so as to absorb 99.9% of incident x rays in the sample. Scattering intensity data were collected by step scanning method using a silicon solid state detector (Kevex Si-SSD) in an energy range of 17.37–17.71 keV. The fixed time and step angle were 200 s, 0.2° for $2\theta = 4°-23°$, 400 s, 0.5° for 18°–80°; and 600 s, 1.0° for 75°–144°, respectively. The incident angle was fixed at 2°. Diffraction angle 2θ ranged 4°–144°, which corresponds to a scattering vector ($Q = 4\pi \sin\theta/\lambda$) of 0.6–16.6 $Å^{-1}$.

After data correction (absorption, polarization, and air scattering) was applied by conventional procedures, the scattering data were normalized by the Krogh-Moe–Norman method[17] and then a structure factor $F(Q)$ was calculated. Residual error correction for $F(Q)$ was performed by Yarnell's method.[18]

D. Reverse Monte Carlo simulation

To obtain the atomic configuration in the sample from the x-ray diffraction data, we employed the reverse Monte Carlo (RMC) method[19] using the RMCA code. In the RMC simulation, $F(Q)$ for the model is represented by the weighted sum of the partial structure factor $A_{ij}(Q)$ as $F(Q) = \Sigma_{ij}\gamma_{ij}A_{ij}(Q)$, where $A_{ij}(Q)$ corresponds to Fourier transform of pair correlation functions $g_{ij}(r)$ of each atom pair and γ_{ij} is coefficient that depends on scattering vector Q defined as $\gamma_{ij} = c_i c_j f_i f_j^* / \Sigma_{ij} c_i c_j f_i f_j^*$, where c_i and f_i are fraction and atom scattering factors for atom species i. The random movements of atoms were generated and the simulation was continued towards reduction of the discrepancy between experimental and calculated $F(Q)$. The initial atomic configuration to be used for RMC simulation was an amorphous structure generated by relaxation of a random configuration using molecular dynamics (MD) simulation.

A starting configuration of 4000 particles with the appropriate composition in which oxygen stoichiometry was determined by charge neutrality was randomly distributed in a cubic box of edge length of ~39 Å with periodic boundary conditions. Applied for the simulation was the atom number density of 0.0678 $Å^{-3}$, which was obtained experimentally from the volume and weight of the films. The starting configuration was then relaxed through classical MD simulation using the code MXDORTO,[20] which is based on two body central force model. The potential parameters were chosen so as to reproduce the structure of crystalline Cd_2GeO_4.[21] The RMC simulation was then carried out to obtain a satisfactory agreement between the x-ray structure factors $F(Q)$ under the following constraints: (i) Ge is fourfold coordinated by O and (ii) the separation of each atom pair is longer than 90% of sum of relevant ionic radii. The simulation was continued until no improvement in the fit between the experimental and calculated $F(Q)$ was observed.

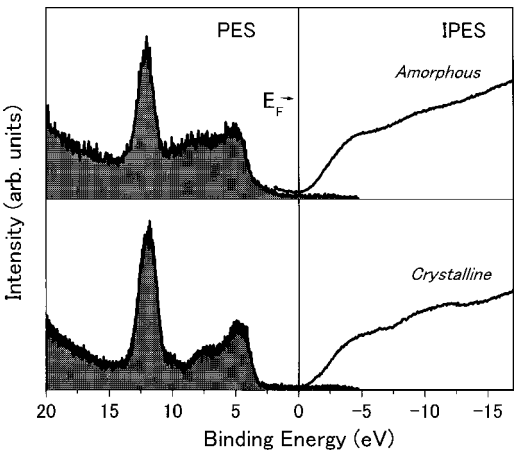

FIG. 2. PE and IPE spectra of amorphous 2 $CdO \cdot GeO_2$ film and polycrystalline bulk Cd_2GeO_4. Intensity of the spectra corresponds to density of states. Fermi level E_F is taken as the origin of the energy axis, which was calibrated using gold. Fermi level is located at the conduction band tail indicating that conductive type is *n* type.

E. Molecular orbital calculation

Molecular orbital calculations were performed by the discrete variational (DV) $X\alpha$ method[22] using the code SCAT.[23] The number of DV sampling points was 1000 per atom. Cd $1s$-$5p$, Ge $1s$-$4p$, and O $1s$-$2p$ were used as atom basis functions. The model cluster $(Cd_9Ge_4O_{37})^{40-}$ was cut from the amorphous structure determined by the RMC simulation under the following conditions: (i) the Cd octahedron is centered in the cluster, (ii) Ge or Cd polyhedra connecting with the Cd octahedron are included, and (iii) other atoms which are located at farther distance are treated as point charges.

Calculations on a $(Cd_9Ge_4O_{40})^{46-}$ cluster that was cut out from the crystalline structure[21] were also carried out for comparison. The model cluster was embedded in an electrostatic potential produced by the point charges outside of the cluster.

III. RESULTS

The analyzed chemical composition of the resulting samples was 63 $CdO \cdot 37\, GeO_2$. Since this composition is close to 2 $CdO \cdot GeO_2$, the composition of the samples is denoted as 2 $CdO \cdot GeO_2$, hereafter, for simplicity.

A. Photoelectron spectra

Figure 2 shows ultraviolet PE and IPE spectra of the amorphous film and the crystalline sample. The spectrum of the amorphous sample is close to that of the crystalline sample with respect to shape and peak position. The value of

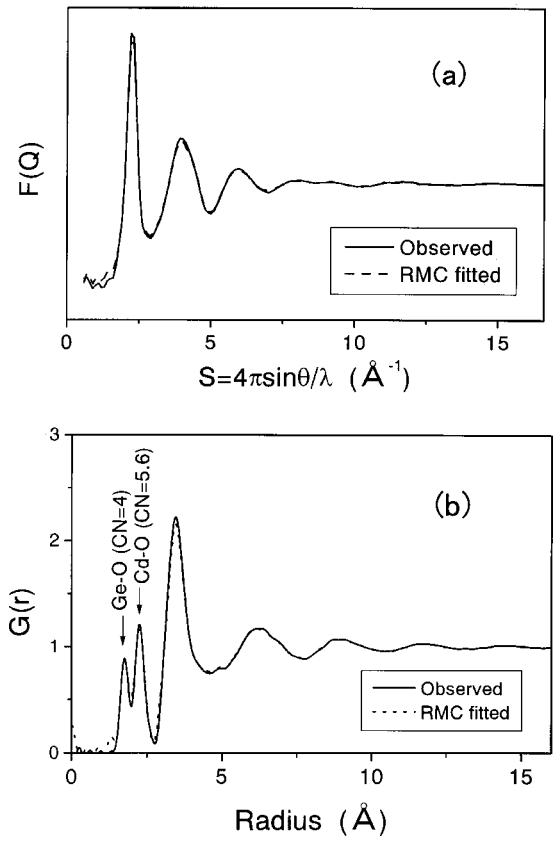

FIG. 3. X-ray diffraction data on amorphous 2 $CdO \cdot GeO_2$. (a) Structure factor $F(Q)$ and (b) radial distribution function $G(r)$ that is Fourier transform of $F(Q)$. The solid curve indicates the experimentally obtained $F(Q)$ or $G(r)$ using Mo $K\alpha$ radiation. A dotted curve denotes the RMC fit of $F(Q)$ and $G(r)$. The final fit was achieved after $\sim 10^6$ steps.

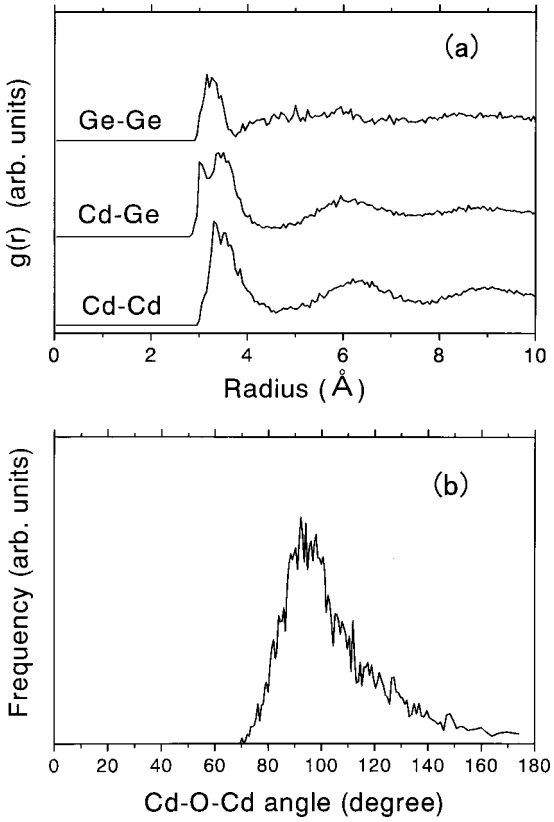

FIG. 4. Correlations in the RMC-fitted structure. (a) Partial pair correlation function $g(r)$ for Ge-Ge, Cd-Ge, or Cd-Cd. Each $g(r)$ function is shifted for clarity. (b) Bond angle correlation for Cd-O-Cd.

the band gap estimated from the DOS separation in the PE-IPE spectra, is ~3.5 eV, which agrees with that (3.4 eV) by optical absorption measurements. It is evident from the figure that the Fermi level is located at the tail of the conduction band. This is direct evidence that the implanted sample is an *n*-type degenerate conductor.

It is noted that when compared with the DOS of the valence-band top the intensity of IPE spectrum, i.e., the DOS of conduction band, increases gradually with increasing energy above the Fermi level. This observation strongly suggests that the conduction band bottom has a large dispersion (i.e., small effective mass) as compared with the valance-band top.

B. X-ray diffraction measurement and RMC simulation

The experimentally obtained structure factor $F(Q)$ is shown in Fig. 3(a) along with the result of the RMC fit. The final fit was achieved after $\sim 10^6$ steps. Figure 3(b) shows the experimental radial distribution function $G(r)$, i.e., Fourier transform of $F(Q)$, together with $G(r)$ deduced from the RMC fit. The first two peaks centered at ~1.7 and ~2.3 Å in $G(r)$ are due to the correlations of the nearest-neighboring Ge-O and Cd-O pairs, respectively. They are located at almost the same distance as those in crystalline Cd_2GeO_4. A good RMC fit was obtained under the constraint of fourfold Ge coordination. The fourfold Ge coordination is based on the observed Raman spectrum of the amorphous film in the previous study.[24] The average oxygen coordination number of Cd in the RMC model was ~5.6, in which the actual distribution was 5 or 6. In the Cd_2GeO_4 crystal, the coordination numbers of O around Ge and Cd are 4 and 6, respectively.

The peak in the range of 3–4 Å in $G(r)$ was due mainly to correlations between cations, such as Cd-Cd, Cd-Ge, and Ge-Ge. Figure 4(a) shows the pair distribution functions $g(r)$ for those atomic pairs. The first peak of Ge-Ge is located at ~3.2 Å, indicating that a fraction of Ge ions is present as polymeric oxides such as $Ge_2O_7^{4-}$, while the crystal Cd_2GeO_4 is composed only of monomeric germanate group GeO_4^{4-}. The $g(r)$ of Cd-Cd has a broad peak centered at ~3.4 Å. The distribution of Cd-O-Cd bond angles is shown in Fig. 4(b). This distribution has a skewed shape. The full width at half maximum (FWHM) is ~30°, and the most probable angle is ~90°, which is close to Cd-O-Cd bond angles in the CdO crystal. The coordination number of cations (Ge or Cd) around O has a distribution with the average value of ~3.6, which is close to the value of 4 in the crystal (O coordinated to one Ge and three Cd's in the crystal).

The nearest-neighbor coordination number and the linkage of the oxygen polyhedra was almost unchanged from the

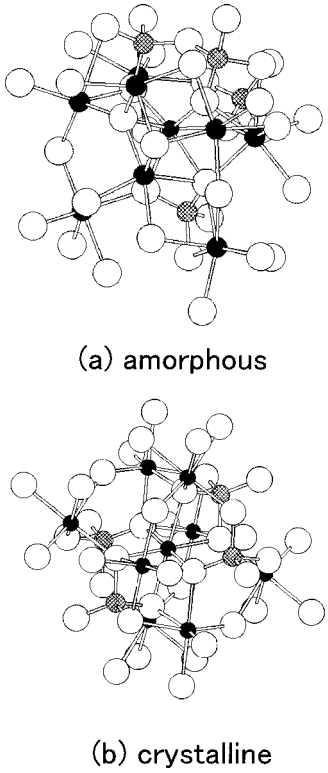

FIG. 5. Model clusters employed for MO calculations. (a) $(Cd_9Ge_4O_{37})^{40-}$ cluster for amorphous phase, (b) $(Cd_9Ge_4O_{40})^{46-}$ cluster for crystal. ● = Cd, ⊗ = Ge, and ○ = O.

starting configuration determined by MD simulation. The actual RMC fit was mainly performed for the metal-oxygen-metal angles. An RMC solution using a starting configuration with a completely random arrangement failed to converge.

C. MO calculation

Figure 5 shows the $(Cd_9Ge_4O_{37})^{40-}$ model cluster for the amorphous phase and $(Cd_9Ge_4O_{40})^{46-}$ for the crystal. In both clusters, the central Cd atom has the same coordination to the other cations, i.e., eightfold coordination for Cd and fourfold for Ge. In the RMC fitted model, each Cd has a variety of coordination numbers but the average value was 7.7 for Cd or 4.3 for Ge. Thus the model clusters may be regarded as representative of the RMC model from the viewpoint of cation coordination. There was a difference in the arrangement of polyhedra between both models. The ''amorphous'' cluster includes a $Ge_2O_7^{4-}$ species while the ''crystalline'' cluster is entirely composed of the monomeric germinate group GeO_4^{4-}. The Cd-Cd distance in the ''amorphous'' cluster was slightly longer than that in the ''crystalline'' cluster.

MO calculations on both model clusters gave almost the same energy level structure. Figure 6 shows density of states for the ''amorphous'' cluster and partial DOS along with the PE-IPE spectrum of the amorphous film. The calculated total DOS reproduces the overall structure of the observed PE-IPE spectrum, and thereby allows us to assign spectral features. For the PE spectrum showing valence band structure, the

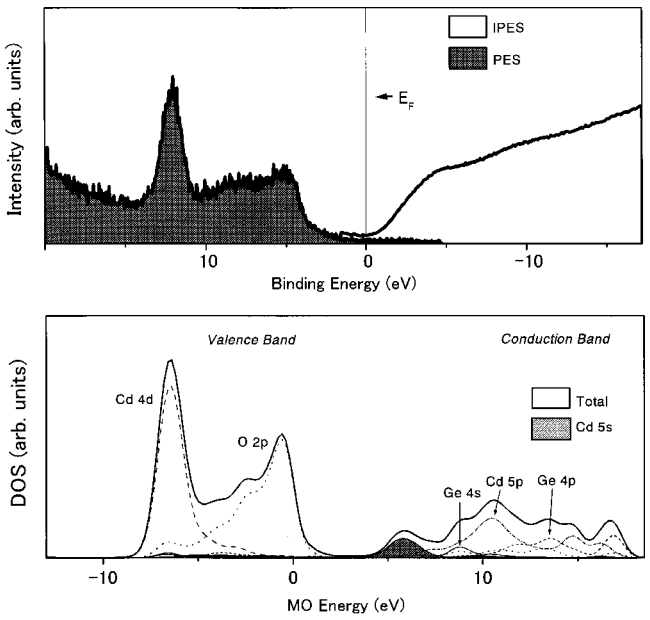

FIG. 6. Calculated DOS for amorphous cluster and its partial components along with the observed PE-IPE spectrum of amorphous 2 $CdO \cdot GeO_2$ film. Drawn was each MO level convoluted by Gaussian function with FWHM of 0.5 eV.

well-resolved and intense peak at binding energy of 13 eV is ascribed to Cd $4d$ and the top of the valence band is primarily composed of O $2p$ orbitals. For the conduction band, Cd $5s$ orbitals contribute largely to the bottom part which controls the electron transport. The center of the Ge $4s$ band is located at an energy higher than that of the Cd $5s$ band. The presence of the $Ge_2O_7^{4-}$ species (dimer) does not make a significant change in the DOS of the conduction band as compared with that in the ''crystalline'' cluster.

Persistent photoconductivity in a-CdO-GeO_2 was observed when the atomic concentration of Cd ions exceeded 50% of all cation sites.[16] The conduction band bottom is substantiated to be primarily composed of Cd $5s$ orbitals by MO calculations, which is consistent with the above observation, indicating that the Cd ions dominate the electrical conduction in this material.

IV. DISCUSSION

A. Electron mobility and physical disorder

The structural analysis revealed that the coordination number of the first neighboring O to Ge or Cd in the amorphous state was close to that in the crystalline state. However, there is a distinct disorder with respect to the medium-range structure in the amorphous state. For example, the interatomic distance of second neighboring atoms, Cd-Cd distance, has a large distribution as compared with those in the corresponding crystalline phase. As is seen in Fig. 3(b), convergence of the oscillation in $g(r)$ beyond $\sim$10 Å is the result of the disappearance of the long-range order.

The direct observation of the conduction band by IPE spectroscopy revealed that there is no substantial difference in the DOS with respect to the energy distribution at the

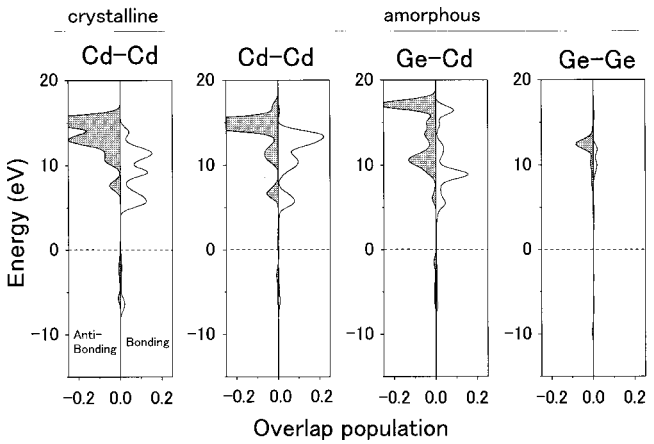

FIG. 7. Bond overlap population diagrams obtained for amorphous and crystalline clusters. The origin of the energy axes corresponds to the valence-band top. The Cd-Cd distance is 3.28 Å in the crystalline or 3.38 Å in the amorphous cluster. Ge-Cd and Ge-Ge distance in the amorphous cluster are 3.06 and 3.45 Å, respectively.

conduction band bottom between the amorphous and the crystalline states. Although the reciprocal space cannot be defined in the amorphous material, the effective mass is a valid concept.[25] Since the electrical conduction of the material is *n* type, the observation by IPE spectroscopy supports an interpretation that the value of the effective mass of carrier electrons in the amorphous state is almost same as that in the crystalline state.

The mobility is defined by the effective mass and mean free path. If carrier concentration is fixed, the latter depends on scattering or relaxation time, which is affected by physical disorder or defects. To say the least, physical disorder does *not* dominate scattering time in the amorphous state of the present material, on the basis of the experimental facts that the electron mobility and the effective mass in the amorphous phase are comparable to those in the polycrystalline form. We consider that such a situation originates from the extended nature of the states at the conduction band bottom.[3] On the basis of the experimental and calculated DOS (Fig. 6), it is now clear that the bottom of the conduction band possesses high Cd 5*s* character.

B. Nature of the conduction band

Figure 7 shows the bond overlap population diagram between two metal ions deduced from Mulliken's population analysis on the model clusters for the amorphous and crystalline states, respectively. The distance between Cd ions is 3.28 Å for the ''crystal'' and 3.38 Å for the ''amorphous'' cluster. As shown in Fig. 7, neighboring Cd 5*s* orbitals are closely overlapped with each other at the bottom of the conduction band, despite the increase in the separation between the Cd^{2+} ions in the amorphous state. The result indicates that the magnitude of the overlap between neighboring Cd 5*s* orbitals is rather insensitive to the neighboring Cd-Cd distance. These features are responsible for the observed large dispersion of the conduction band even in the amorphous state.

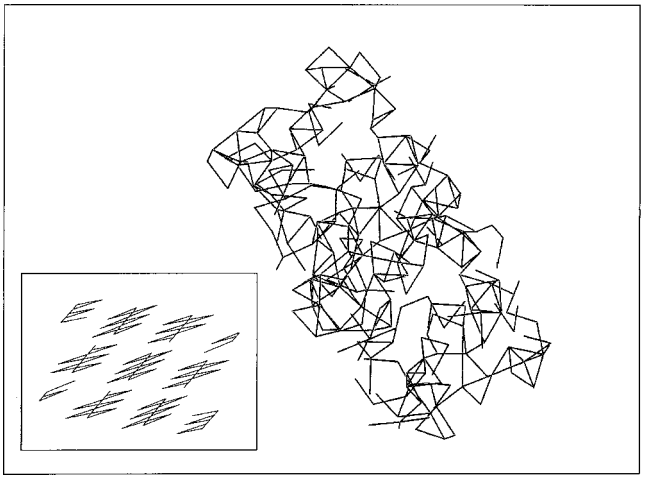

FIG. 8. Cd-Cd correlations extracted from the resulting RMC model for amorphous 2 $CdO \cdot GeO_2$. The representation is $\frac{1}{8}$ of the actual RMC box. When the neighboring Cd-Cd separation is within the sum (3.6 Å) of two Cd^{2+} 5*s* orbital radii, a pair of Cd ions is connected by a line. Note that 3D-percolation pathways for electrons are seen in whole configuration space. The inset is the figure drawn by the same procedure for crystal.

The Ge-Cd bonding state also significantly contributes to the conduction band bottom because of short distance (3.06 Å). On the other hand, the contribution of the Ge-Ge bonding state is very small, indicating that the Cd ion is indispensable for the extended conduction band bottom.

Figure 8 shows Cd-Cd correlations extracted from the RMC model along with those of crystal. Lines connect neighboring Cd^{2+} ions which are separated by less than 3.60 Å (twice Slater's radius of Cd^{2+} 5*s* orbital). It is evident from the figure that (i) a regular pattern is drawn for the crystalline state, while, on the contrary, zigzag-chains are formed for the amorphous state and (ii) even in the amorphous state, continuous Cd-Cd connections are clearly seen through the RMC model structure. The latter indicates that Cd 5*s* orbitals percolate through the amorphous state, leading to extended electronic states at the conduction band bottom.

Figure 9 shows the contour maps of the wave functions at

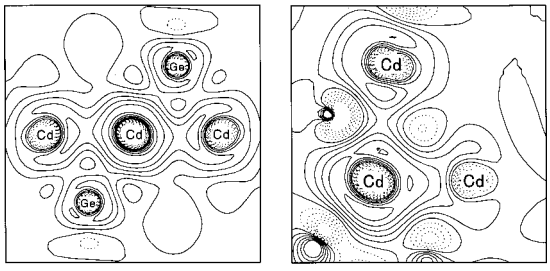

FIG. 9. Contour map of wave function near the bottom of the conduction band for (a) crystalline and (b) amorphous cluster. Each wave function is primarily composed of Cd 5*s* atomic orbitals and delocalization of the wave functions is seen along with the Cd chain.

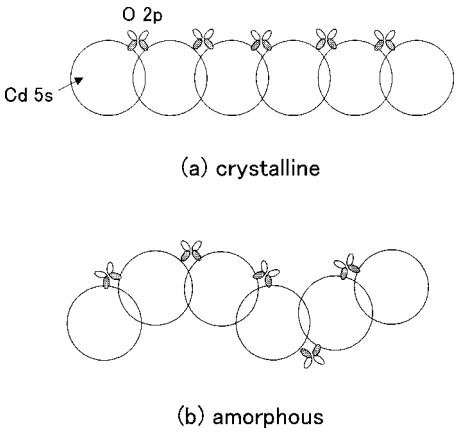

FIG. 10. Schematic representation of orbital drawing of conduction band bottom for (a) crystalline and (b) amorphous state of $2\,CdO\cdot GeO_2$.

the bottom of the conduction band for the ''crystalline'' and ''amorphous'' clusters. A plane including a Cd ion chain was chosen for the crystalline. For the amorphous, a plane including three Cd ions was selected. Delocalization of the wave function with high Cd $5s$ character over three Cd^{2+} ions is observed even in the amorphous state. A difference between the crystalline and amorphous states is significant admixture of Ge $4s$ to the conduction band bottom in the former.

Figure 10 schematically illustrates the bottom of the conduction band in the materials from viewpoint of chemical bonding. In the crystalline state, each Cd ion connects via O ions, and the Cd ions line up and the Cd $5s$ orbitals are closely overlapped [Fig. 10(a)]. On the other hand, in the amorphous state, although disorder in the arrangement of Cd ions arises and zigzag structures are formed [Fig. 10(b)], the overlaps of the relevant Cd $5s$ orbitals still remain at a level comparable to those in the crystalline state since they are insensitive to disorder, such as a fluctuation of Cd-O-Cd bond angles. We consider that the origin of the extended electronic states at the conduction band bottom is the insensitivity in the magnitude of the overlap of neighboring Cd $5s$ orbital to the structural fluctuation. The present results support the experimental fact that electron mobility in this material is not significantly influenced by structural disorder. The situation makes a contrast with the case of the *s* orbitals of metal cation with smaller principle quantum number or the *p* orbitals having spatial anisotropy, in which the magnitude of the overlap is small or sensitive to disorder. For example, the electron mobility in *a*-Si:H is lower by several orders of magnitude that in crystalline Si.

C. Electron carrier generation

Ion implantation is an established method for carrier doping into crystalline Si and GaAs. We have reported that the ion implantation technique is effective in generating carrier electrons in a crystalline TCO, $MgIn_2O_4$, with a high efficiency rate of ~20% for the as-implanted sample and ~40% for the annealed sample.[26,27] The carrier generation efficiency of amorphous $2\,CdO\cdot GeO_2$ is ~10% in the as-implanted state, which is smaller than that of crystalline $MgIn_2O_4$, but it is noteworthy that ion implantation is effective for carrier generation even in the amorphous oxide.

The electron carrier generation process via ion implantation of protons in the present material has a several possibilities. The possibility of substitutional doping as in crystalline semiconductors is not consistent with the experimental result that the material is *n*-type. Otherwise, the substitution of protons for Cd^{2+} or Ge^{4+} ions should lead to *p*-type conduction. Formation of oxygen-ion vacancies by simple nuclear collisions during the ion implantation is another possible channel. No change in conductivity was observed in the He^+-implanted film.[3] Therefore, this channel is not dominant in the H^+-implanted film because of the smaller mass of H than He. Also, we must consider the possibility that the implanted H chemically reduces Cd^{2+} or Ge^{4+} ions in the film. Chemical reduction leads to the formation of suboxide of CdO or GeO_2, which gives visible coloration. However, the reduction of optical transparency in the visible region was very small upon the ion implantation. This observation indicates that chemical reduction effects are not dominant at the present fluence level. The estimation that the carrier generation was performed by interstitial (chemical) doping has more possibility as compared with the above three channels. Interstitial doping is also reported in Li^+-implanted amorphous Si.[28]

Finally, let us discuss the carrier generation in the material based on the structural information. The average coordination number is deduced to be 4.2 from the RMC model, including the value of ~3.6 for O, which is rather large compared to conventional glass. For example, the average coordination number is 2.67 for a-SiO_2 or 2.4 for a-As_2S_3. A high coordination number is likely to be favorable for the generation of carrier electrons since the carrier doping may be regarded as an excitation of electrons by the rigidity of the network. The main reason for the difficulty of carrier doping in amorphous materials is its structural flexibility, in our opinion.

V. CONCLUSION

The electronic structure of a-$2\,CdO\cdot GeO_2$, a transparent conductive amorphous oxide, was examined by photoelectron and inverse-photoelectron spectroscopy and molecular orbital calculations on model clusters which were cut from the amorphous structures justified by x-ray diffraction analysis combined with molecular dynamics and reverse Monte Carlo simulations. The oxygen coordination numbers around Cd^{2+} and Ge^{4+} are ~6 and ~4, respectively, and these values are close to those in crystalline Cd_2GeO_4. The conduction band bottom controlling electron-transport properties is primarily composed of Cd $5s$ orbitals, and the magnitude of the overlap between neighboring Cd $5s$ orbitals is large and almost the same as that in the crystalline state. This unique feature originates for two reasons. One is the highly ionic nature of Cd-O bonding. The bond angle of Cd-O-Cd is close to that (90°) of the CdO crystal. Thus, the Cd-Cd separation is rather short compared with that in covalent systems. Another is the large spatial (spherical) spreading of the Cd $5s$ orbital. The magnitude of the overlap between the neighbor-

ing Cd 5*s* orbitals is large and insensitive to the fluctuation of the Cd-O-Cd bond angle which characterizes the amorphous state. As a consequence, the electron mobility ($\sim$10 $cm^2 V^{-1} s^{-1}$) is not drastically degraded in the amorphous state as compared with that in the crystalline state. The mean free path estimated from the mobility is $\sim$1 nm, which is rather larger than the interatomic distance. This fact may explain the absence of the *pn* anomaly in the Hall coefficient in this material because this anomaly results from the mean free path being comparable to the interatomic spacing.

The conductivity of *d*-electron metals does not drop drastically upon melting or amorphization. Since a *d* orbital has three lobes, it is close to spherical in shape and each metal atom directly contacts with other metals without intervening oxygen. In heavy-metal oxide systems, although the topological sequence of the ion arrangement is metal-oxygen-metal, the conduction band bottom is primarily composed of vacant *s* orbitals of the heavy metal cations and the contribution of the intervening oxygen is rather small. Therefore, we may regard that series of transparent conductive amorphous oxides have a similarity to amorphous metals except for optical transparency.

ACKNOWLEDGMENTS

The authors would like to thank Dr. J. Jisun and Professor T. Yoko of Kyoto University for their help with the x-ray diffraction measurements.

*Corresponding author. Author to whom correspondence should be addressed. Email address: hosono2@rlem.titech.ac.jp

[1] C. W. Ow-Yang, D. Spinner, Y. Shigesato, and D. Paine, J. Appl. Phys. **83**, 145 (1998).
[2] M. Yasukawa, H. Hosono, N. Ueda, and H. Kawazoe, Jpn. J. Appl. Phys., Part 2 **34**, L281 (1996).
[3] H. Hosono, N. Kukuchi, N. Ueda, H. Kawazoe, and K. Shimizu, Appl. Phys. Lett. **67**, 2663 (1995).
[4] H. Hosono, Y. Yamashita, N. Ueda, H. Kawazoe, and K. Shimizu, Appl. Phys. Lett. **68**, 661 (1996).
[5] M. Orita, H. Ohta, M. Hirano, S. Narushima, and H. Hosono, Philos. Mag. B **81**, 501 (2000).
[6] Z. Ovadyahu, J. Phys. C **19**, 5197 (1986).
[7] J. R. Bellingham, W. A. Phillips, and C. J. Adkins, J. Phys.: Condens. Matter **2**, 6207 (1990).
[8] B. Pashmakov, B. Claflin, and H. Fritzsche, J. Non-Cryst. Solids **164**, 441 (1993).
[9] S. Narushima, H. Hosono, J. Jisun, T. Yoko, and K. Shimakawa, J. Non-Cryst. Solids **274**, 313 (2000).
[10] M. Burman, J. Hirsch, and T. Ramdeen, J. Phys. C **14**, 117 (1981).
[11] T. Tiedje, J. M. Cebulka, D. L. Morel, and B. Abeles, Phys. Rev. Lett. **46**, 1425 (1981).
[12] E. R. Whipple, S. N. Subbarao, and F. P. Koffyberg, J. Solid State Chem. **34**, 231 (1980).
[13] K. Shimakawa, S. Narushima, H. Hosono, and H. Kawazoe, Philos. Mag. Lett. **79**, 755 (1999).
[14] N. F. Mott and E. A. Davis, *Electronic Processes in Non-Crystalline Materials*, 2nd ed. (Clarendon, Oxford, 1979), p. 161.
[15] *The Stopping and Range of Ions in Solids*, edited by J. F. Ziegler (Pergamon, New York, 1985).
[16] N. Kikuchi, H. Hosono, H. Kawazoe, K. Oyoshi, and S. Hishita, J. Am. Ceram. Soc. **80**, 22 (1997).
[17] J. Krogh-Moe, Acta Crystallogr. **9**, 351 (1956); N. Norman, *ibid.* **10**, 370 (1957).
[18] J. L. Yarnell, M. J. Kartz, and R. G. Wenzel, Phys. Rev. A **7**, 2130 (1973).
[19] R. L. McGreevy and L. Pusztai, Mol. Simul. **1**, 359 (1998).
[20] K. Kawamura (unpublished).
[21] E. L. Belokoneva *et al.*, Sov. Phys. Crystallogr. **18**, 610 (1974).
[22] H. Adachi, M. Tsukada, and C. Satoko, J. Phys. Soc. Jpn. **45**, 875 (1978).
[23] D. E. Ellis, H. Adachi, and F. W. Averill, Surf. Sci. **58**, 497 (1976).
[24] H. Hosono, M. Yasukawa, and H. Kawazoe, J. Non-Cryst. Solids **203**, 334 (1996).
[25] S. Kivelsen and C. D. Gelatt, Jr., Phys. Rev. B **19**, 5160 (1979).
[26] H. Kawazoe, N. Ueda, H. Un'no, H. Hosono, and H. Tanoue, J. Appl. Phys. **76**, 7935 (1994).
[27] H. Hosono, N. Ueda, H. Kawazoe, and N. Matsunami, J. Non-Cryst. Solids **182**, 109 (1995).
[28] W. Beyer and R. Fischer, Appl. Phys. Lett. **31**, 850 (1977).